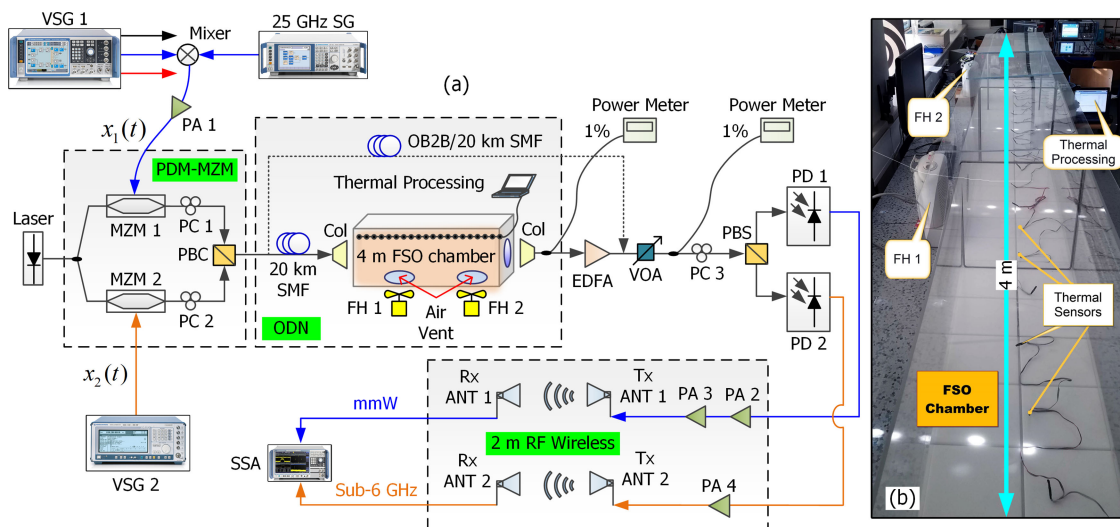**Open Access**

Polarization Division Multiplexing-Based Hybrid Microwave Photonic Links for Simultaneous mmW and Sub-6 GHz Wireless Transmissions

Dong-Nhat Nguyen, *Member, IEEE*
Jan Bohata
Jan Spacil
Matej Komanec
Nobby Stevens
Zabih Ghassemlooy, *Senior Member, IEEE*
Pham Tien Dat, *Member, IEEE*
Stanislav Zvanovec, *Senior Member, IEEE*

Polarization Division Multiplexing-Based Hybrid Microwave Photonic Links for Simultaneous mmW and Sub-6 GHz Wireless Transmissions

Dong-Nhat Nguyen ©,[1] *Member, IEEE*, **Jan Bohata** ©,[1] **Jan Spacil**,[1]
Matej Komanec ©,[1] **Nobby Stevens** ©,[2]
Zabih Ghassemlooy ©,[3] *Senior Member, IEEE*,
Pham Tien Dat ©,[4] *Member, IEEE*,
and **Stanislav Zvanovec** ©,[1] *Senior Member, IEEE*

[1]Department of Electromagnetic Field, Czech Technical University in Prague, Prague 16627, Czech Republic
[2]ESAT-DRAMCO, KU Leuven, Leuven 3000, Belgium
[3]Optical Communication Research Group, Faculty of Engineering and Environment, Northumbria University, Newcastle upon Tyne NE1 8ST, U.K.
[4]Network System Research Institute, National Institute of Information and Communication, Tokyo 184-8795, Japan

Abstract: A new hybrid microwave photonic link based on a polarization division multiplexing Mach-Zehnder modulator (PDM-MZM) is proposed. The link enables co-transmission of millimeter-wave (mmW) and sub-6 GHz wireless signals over a seamless single-mode fiber (SMF) and free-space optics (FSO) channels. Optimization of the chromatic dispersion (CD)-induced power fading regardless of the power fading due to the non-deterministic atmospheric turbulence (AT) is simultaneously demonstrated. Extensive simulation analysis is first presented to examine (i) the impact of CD on mmW (25 GHz) and sub-6 GHz (2.6 GHz) signals, envisioned for the 5th generation networks, and (ii) optimization of CD-induced power fading by changing the phase relations between the optical carrier and optical sidebands in each polarization channel using single tunable polarization controller. A proof-of-concept experiment is finally performed to simultaneously deliver 25 GHz and 2.6 GHz signals with 4/16/64-quadrature amplitude modulation over (i) 20 km SMF and 2 m radio wireless link and (ii) 20 km SMF, 4.2 m FSO (with AT) and 2 m radio wireless links. The optimization of the CD-induced power fading is experimentally verified and link performance shows high tolerance to CD with no power penalties and the measured error vector magnitudes well below the required limits. The predicted bit error rates are also below the forward error correction threshold of 2×10^{-4}.

Index Terms: Millimeter-wave, sub-6 GHz, multi-RAT, radio-over-fiber, free-space optics, microwave photonic link.

1. Introduction

The data traffic on wireless communications is growing exponentially due to the use of ever-increasing number of devices, e.g., smartphones, laptops, tablets, etc., requiring access to multi-Gb/s bandwidth-demanding applications and services. The sub-6 GHz radio access technology (RAT) has been developed for the 5th generation (5G) wireless networks to address this demand [1], [2]. These sub-6 GHz bands offer promising attributes for mobile broadband and possess interesting propagation characteristics to support wide area coverage. However, to support the growing demand for the bandwidth, the communication industry is moving to the higher radio frequency (RF) range in the millimeter-wave (mmW) bands, e.g., mmW RAT [3]. In 2016, the Federal Communications Commission officially announced the frequency slots in the mmW bands of $24.75 - 25.25$, $27.5 - 28.35$, $38.6 - 40$ and $57 - 71$ GHz as part of 5G [4]. In early 2020, Global System for Mobile Communications Association updated the 5G spectrum public policy position with the emphasizes on 26, 28 and 40 GHz frequencies, which has currently received the most international support and strong momentum from operators due to the widest harmonization with minimized user equipment complexity [2].

Despite the fact that the mmW frequency bands are capable of offering ultra-high broadband services, i.e., multi-Gb/s data rate (R_b), which is envisioned for the broadband access network in 5G, the high signal attenuation due to the atmospheric condition (gaseous, rain, snow, turbulence, etc.) limits the transmission range d. For example, a 28 GHz mmW point-to-point communication system was demonstrated in [5] with R_b of 2 Gb/s at d of 1 km, which implies that only users close to the cell site will receive the full benefit of mmW-based wireless service. In addition, mmW signals are unable to penetrate most solid materials very well, since they are more susceptible to blockages such as walls, buildings and trees. E.g., at 40 GHz the signal attenuation through 10 cm concrete materials is 175 dB compared to $\sim$18 dB at sub-6 GHz (i.e., < 3 GHz) [5].

Therefore, to (*i*) reuse the transport networks of current sub-6 GHz RAT for the new mmW RAT and (*ii*) offer more widespread 5G deployments for supporting all use cases at a low cost and reduced time, co-transmission of the sub-6 GHz and mmW wireless signals over the current mobile transport i.e., mobile fronthaul/backhaul are highly desirable and attractive. The microwave photonic link (MPL), i.e., radio-over-fiber, has been represented as an attractive alternative technology with numerous advantages such as low attenuation, ultra-broad bandwidth, excellent flexibility and immunity to RF electromagnetic interference [6]–[10]. In the centralized radio access network architecture using MPL, multiple RF signals are generated at the central station (CS) and directly transmitted to the base station (BS) via an optical distribution network (ODN), e.g., optical fiber, with no protocols and interfaces modifications and therefore significantly reducing cell site hardware complexity and cost [11]. At the BS, the received multiple RF signals are electrically amplified and then radiated via antennas (ANTs) to the user equipment. Furthermore, as demonstrated in [12], the MPL is also applicable for the implementation of multiple-input multiple-output technology, which increases the link capacity enormously.

The simplest method for simultaneous transmission of mmW and sub-6 GHz wireless signals is to employ the MPL-based wavelength-division-multiplexing technology. However, assigning an optical wavelength per RAT is a costly and bulky solution due to the use of multiple optical transmitters (Txs) and receivers (Rxs), i.e., lasers, optical modulators and high-speed photodetectors (PDs) [13]. It is worth mentioning that high-speed PDs are relatively expensive; they however can be reused for future wireless networks, where mmW RATs are widely operated. In addition, with the on-going development of optoelectronic devices and integration technologies, commercial high-speed PDs (i.e., > 20 GHz bandwidth) could become more cost-effective in the next few years. Therefore, the option of adopting MPL for supporting multi-RAT in a compact and cost-effective manner using only a single laser would be highly desirable. There are two possible solutions, which have been proposed and demonstrated recently using:

1) Subcarrier multiplexing via an electrical combiner [14], [15]. This solution is simple and cost-effective. However, the intermodulation distortion owing to the combination of two electrical signals is high and more importantly, the effect of fiber chromatic dispersion (CD) is severe,
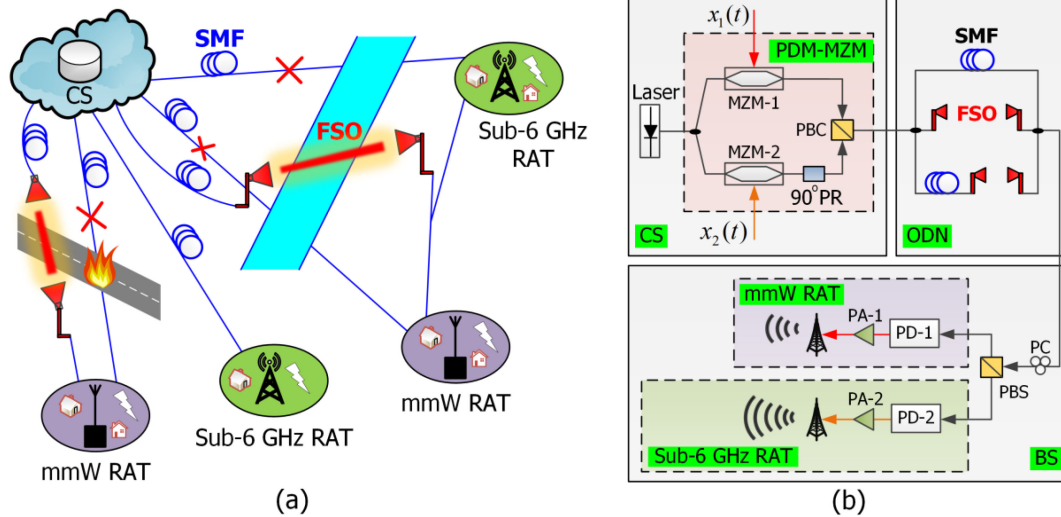
Fig. 1. (a) A converged fiber-FSO-wireless systems for 5G and beyond networks and (b) schematic of the proposed system with PDM-MZM for the co-transmission of mmW and sub-6 GHz signals.

especially for the mmW signal when simple optical double-sideband (DSB) modulation is employed [14].

2) Dual-drive MZM technique [16], [17]. This approach requires the optimization of both bias voltages applied to the dual-drive MZM and an optical interleaver to separate the multi-RF signals [17].

In these works, only a single-mode fiber (SMF) channel was employed for the signal transmission. In addition, no sub-6 GHz wireless link was carried out. In this work, for the first time, to the best of our knowledge, we propose and experimentally demonstrate the co-transmission of mmW (i.e., 25 GHz) and sub-6 GHz (i.e., 2.6 GHz) signals based on the polarization division multiplexing-MZM (PDM-MZM) technique over two configurations of ODN, which consists of (*i*) only a SMF channel, namely PDM-MPL and (*ii*) a hybrid optical link (i.e., of SMF and FSO) known as PDM-hybrid microwave photonic link (PDM-HMPL) under atmospheric turbulence (AT).

Note that, in ultra-dense urban areas, the deployment of optical fiber cables is costly, complex and requires the right of access. Therefore, in such cases as well as in areas where there are very limited coverage or no coverage at all due to damaged optical fibers or environmental disasters, the FSO technology could be deployed at reduced cost and time to provide flexible wireless services prior to the final RF transmission from nodes to users, see Fig. 1(a). However, both RF (especially mmW) and optical signals will experience attenuation and distortions imposed by the channels. In the SMF channel, CD is more severe for the DSB-based modulation scheme because of the relative phase changes between the optical carrier (f_{oc}) and sidebands (f_{sb}) frequencies, which will seriously deteriorate the quality of transmission signals [18]. In the FSO channel, the propagating signal will experience both attenuation and fluctuations due to fog and AT. The latter is due to random small-scale temperature variations along free-space channel, which results in changes of the refractive index and thus irradiance variations [19]. These detrimental effects lead to an extremely low received RF power (P_{rRF}) level at the Rx, thus resulting in a reduction of demodulated signal quality in terms of distorted quadrature amplitude modulation (QAM) constellation diagrams, high error vector magnitude (EVM) and bit error rate (BER). In this work, to compensate for the CD-induced relative phase changes, we propose a simple technique based on a tunable polarization controller (PC) at the BS to adjust the phase of f_{oc}. By properly controlling the PC, the CD-induced power fading on RF wireless signals are optimized independently regardless of the AT-induced power fading effect. We have observed no performance degradation due to CD for mmW and sub-6 GHz signals using the optical DSB modulation. By adopting the proposed scheme, P_{rRF} is

maintained at the desirable level with discernible constellation diagrams and improved EVM and BER without employing complex high-speed digital signal processing [20]. This, ultimately, leads to the reduced complexity and cost of the transport system.

It is worth to mention that, in [18] tunable PCs were used to optimize the CD-induced power fading in 6 GHz MPL. Two tunable PCs were employed since the two vector signals at the Tx were independently intensity- and phase-modulated by a complex in-phase-quadrature MZM, which consisted of 4 phase modulators and a polarization rotator (PR). However, no work has been reported on the hybrid SMF-FSO and RF wireless system.

The remainder of this paper is structured as follows. Section 2 describes the proposed system and provides simulation analysis on the simultaneous transmission of 5G-envisioned mmW and sub-6 GHz signals and the CD-induced power fading optimization. Section 3 describes the proof-of-concept experimental setup, while Section 4 discusses the extensive experimental results. Finally, Section 5 outlines the conclusions of the work.

2. Operating Principle and Simulation Analysis

2.1 Link Structure

The schematic diagram of the proposed system is shown in Fig. 1(b). At the CS, the laser output at a central wavelength of 1550 nm is equally split into two branches, which are applied to two MZMs for external modulation by the mmW $x_1(t)$ and sub-6 GHz $x_2(t)$ signals via the RF input ports of the MZM-1 and MZM-2, respectively. To ensure orthogonality of both polarization states, a PR at the output of MZM-2 is used to rotate the state of polarization of the optical signal by 90°. Both optical signals are subsequently multiplexed using a polarization beam combiner (PBC), the output of which is transmitted to ODN via a SMF. Note that, the PDM-MZM is a commercially available integrated device, as recently demonstrated in [21].

In ODN, the polarized optical signal can be transmitted via three paths of (*i*) SMF, (*ii*) FSO, and (*iii*) hybrid SMF-FSO. Next, the output of ODN is applied to two Rxs at the BS via the tunable PC, which is employed to optimize the CD-induced power fading, and a polarization beam splitter (PBS). The regenerated $x_1(t)$ and $x_2(t)$ signals are further amplified using power amplifiers (PAs) prior to being wirelessly transmitted via commercial ANTs.

2.2 Simulation Results

For the initial link analysis, we first use OptiSystem-MATLAB co-simulation platform to evaluate the performance of the simultaneous transmission of mmW and sub-6 GHz signals over the SMF channel. Since the distance of 5G optical fronthaul links between CS and BS is typically below 20 km, we consider 10 and 15 km of SMF to represent practical links. As a benchmark, the optical back-to-back (OB2B) link (i.e., no ODN) is also considered. Note that, the optical power at the output of the PDM-MZM is set at 0 dBm. We first investigate the co-transmission of $x_1(t)$ and $x_2(t)$ signals, i.e., 25 and 2.6 GHz 4-QAM, respectively at R_b of 4 Gb/s (2 GHz bandwidth) with the input RF power levels of 10 and 0 dBm, respectively. To assess the impact of CD, we have not used PC. Fig. 2(a–c) depicts the simulated optical spectra for x_1 and x_2-polarization multiplexed signals at the input of PD-1 for OB2B, 10 and 15 km SMF, respectively. As can be seen in Fig. 2(a), the optical spectra clearly show the DSB intensity-modulated scheme for $x_1(t)$ with 25 GHz frequency spacing from the optical-data-tone to f_{oc}. However, for the cases of 10 and 15 km SMFs, see Figs. 2(b) and (c), we observe not only the reduction in optical power of $x_1(t)$ compared with OB2B but also the optical signal leakage of $x_2(t)$ (i.e., 2.6 GHz carrier component). This is due to the crosstalk between the two polarizations in a PDM system over a long SMF. The longer SMF distances, the more pronounced leakage, which in turn, leads to polarization misalignment and especially, the CD-induced power fading effect at the Rx. However, by controlling the PC, we can flexibly adjust the polarization misalignment between the optical signals from the two MZMs and compensate for the CD [18].
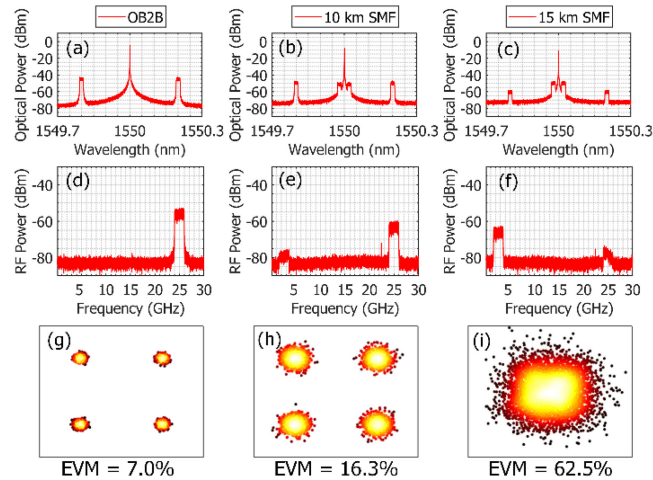
Fig. 2. Simulated optical spectra (a–c); received electrical spectra (d–f); and constellation diagrams of the $x_1(t)$–25 GHz 4-QAM signal (g–i) for OB2B, 10 and 15 km SMF links.
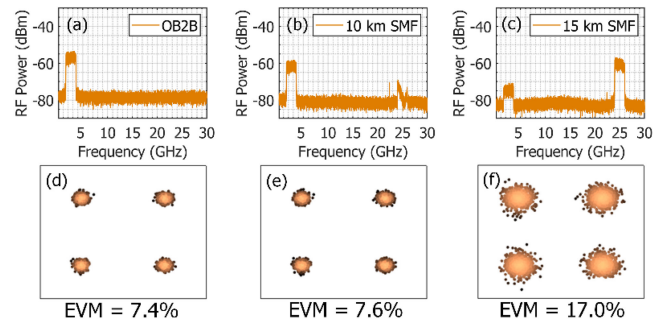

Fig. 3. Simulated received electrical spectra (a–c); and constellation diagrams of the $x_2(t)$–2.6 GHz 4-QAM signal (d–f) for OB2B, 10 and 15 km SMF links.

Fig. 2(d–f) depicts the corresponding spectra of the electrical signals at the output of PA-1 for OB2B, 10 and 15 km SMF links. Note that, for 15 km SMF, P_{rRF} of $x_1(t)$ is reduced by 22 and 15 dB compared with OB2B and 10 km SMF, respectively. The constellation diagrams for OB2B, 10 and 15 km SMF links are illustrated in Fig. 2(g–i). For the OB2B and 10 km SMF links, the EVM values are 7.0 and 16.3%, respectively, which are below the 17.5% EVM requirement. For the 15 km SMF link, it is not possible to demodulate the signal due to the significant reduction of received power.

Similarly, Fig. 3 depicts the performance of the $x_2(t)$, where the spectra at the output of PA-2 for OB2B, 10 and 15 km SMF links are shown in Fig. 3(a–c). We also observe the inter-channel interference from $x_1(t)$ (i.e., 25 GHz carrier component) following transmission over 10 and 15 km SMFs. The constellation diagrams depicted in Fig. 3(d–f) show reduced distortions compared with Fig. 2(g–i). However, unlike $x_1(t)$, the effect of CD-induced power fading on $x_2(t)$ is less severe since the signal power periodically fades with the increasing of the carrier frequency [18]. The EVM values for OB2B, 10 km and 15 km SMF links are 7.4, 7.6 and 17.0%, which are below the 17.5% EVM level.

2.3 Optimization of the CD-induced Power Fading

In the previous section, we investigated the effect of CD-induced power fading due to the relative phase changes between f_{oc} and f_{sb} for mmW and sub-6 GHz signals. However, the phase difference can be tuned using a tunable PC at an angle of ϕ and thus the compensation of power fading for $x_1(t)$ and $x_2(t)$ can be achieved. The results are depicted in Fig. 4.
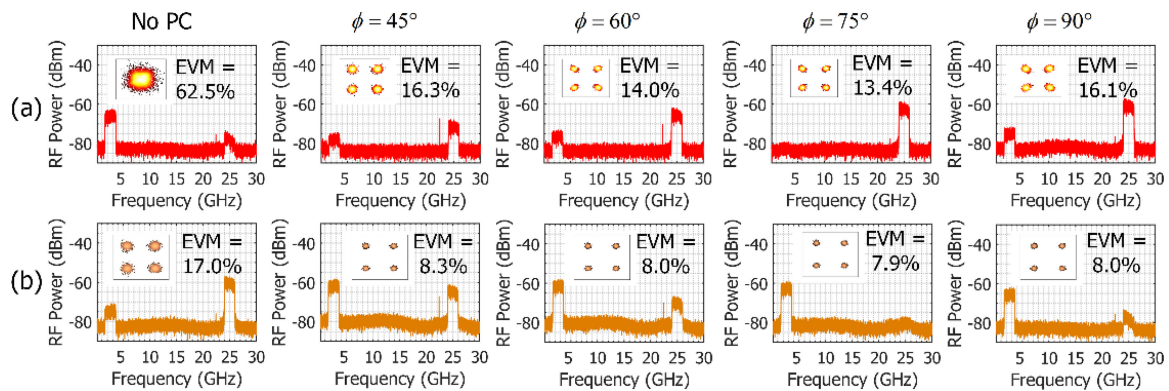
Fig. 4. Simulated received electrical spectra of: (a) $x_1(t)$ and (b) $x_2(t)$ for different PC angles for 15 km SMF transmission. Insets are the corresponding constellation diagrams.

As shown previously, for $x_1(t)$ with no tunable PC we observe significantly reduced P_{rRF} and the presence of $x_2(t)$ following transmission over a 15 km SMF link. However, using a tunable PC with ϕ set within the range of 45°–90° (at a step of 15°), the effect of power fading for $x_1(t)$ is gradually improved and the optimum P_{rRF} of −60 dBm is achieved at ϕ of 75°, see Fig. 4(a). Note that, by controlling the PC, the existence of $x_2(t)$ is simultaneously suppressed. At ϕ of 75° the constellation diagram is stable with an EVM of 13.4%, which is well below the 17.5% EVM level for 4-QAM. Similar for $x_2(t)$, see Fig. 4(b), at ϕ of 75° we observe (*i*) full recovery of $x_2(t)$ with reduced interference (i.e., 19 dB) due to $x_1(t)$ and (*ii*) a clear constellation diagram with the best EVM of 7.9% (i.e., 9.1% EVM improvement in comparison to the case with no PC). It is worth mentioning that the EVM performance of both $x_1(t)$ and $x_2(t)$ can be further improved by suitably increasing the input RF power. This is important because higher signal bandwidth and modulation formats (i.e., 256-QAM) with the low required EVM limit of 3.5% are considered in future wireless networks.

3. Experimental Setup

A complete experimental proof-of-concept system schematic is shown in Fig. 5(a). A continuous wave from the laser source (ID Photonics Cobrite-DX4) is applied to a PDM-MZM module, which is composed of two zero-chirp single-drive MZMs (MZM-1–Fujitsu FTM7938EZ/210 and MZM-2–Covega Mach-10^{TM} 081), via a 50/50 coupler.

Because of the equipment limitation, we could generate relatively narrow bandwidth signals and transmit them over the system to prove the proposed concept. Different modulations i.e., 4-, 16- and 64-QAM with a bandwidth range of 5 to 20 MHz can be adaptively configured. However, for the upper branch, we investigate only the maximum signal bandwidth of 20 MHz for 4/16/64-QAM with the corresponding highest R_b of 40, 80 and 120 Mb/s, respectively [22], which are generated by a vector signal generator (VSG-1–R&S SMW200A). These are the evolved universal terrestrial radio access 3.3, 3.2 and 3.1 test models, respectively as defined by the standard. The mmW signal $x_1(t)$ is then electrically up-converted to 25 GHz using a signal generator (R&S SMF100A) via an electronic mixer prior to being amplified by a power amplifier (PA-1–Wisewave AGP-33142325-01) to a level of 10 dBm. For the lower branch, the sub-6 GHz signal $x_2(t)$, i.e., the 4/16-QAM microwave vector signals with the carrier frequency and signal bandwidth of 2.6 GHz and 17 MHz, is generated using a VSG-2 (R&S SMIQ3B). Note that, for 4- and 16-QAM R_b values are 34 and 68 Mb/s, respectively, and the input RF power of $x_2(t)$ is set to 0 dBm.

The outputs of externally modulated MZMs are applied to two PCs, which are properly adjusted to achieve the desired orthogonal state of polarization prior to being multiplexed using a PBC for transmission over (*i*) a 20 km SMF and (*ii*) a hybrid SMF-FSO link i.e., 20 km and 4.2 m, respectively. Considering that the optical power measured after the PBC is 0 dBm, the optical
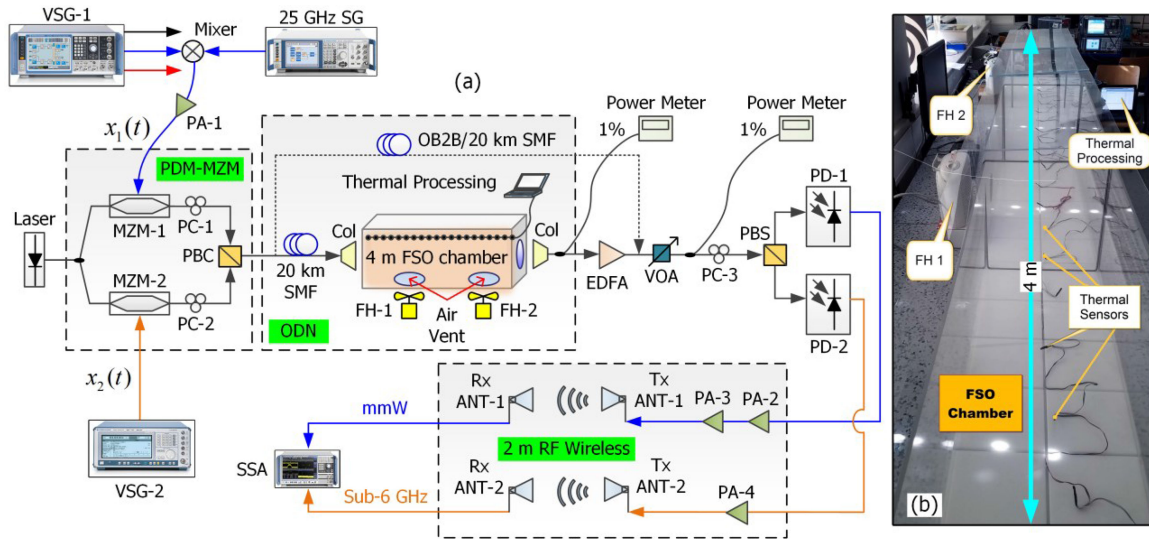
Fig. 5. (a) Experimental setup and (b) turbulent FSO chamber. MZM: Mach-Zehnder modulator, PC: polarization controller, PBC: polarization beam combiner, SMF: single-mode fiber, FSO: free-space optics, FH: fan heater, Col: collimator, EDFA: erbium-doped fiber amplifier, VOA: variable optical attenuator, PD: PIN photodiode, PA: power amplifier and ANT: antenna.

nonlinear effect in SMF therefore can be neglected. For the FSO link, we used (*i*) a pair of air-spaced doublet collimators (Col–Thorlabs F810APC-1550) and (*ii*) an indoor atmospheric turbulent chamber with a dimension 4 × 0.4 × 0.4 m, see Fig. 5(b), to investigate the impact of AT on the signal quality. Note that, the AT strength is usually characterized by the refractive index structure parameter C_n^2 (m$^{-2/3}$) ranging from 10^{-17} to 10^{-13} m$^{-2/3}$ for weak-to-strong AT regimes in outdoor environments [23]. To generate AT within the chamber, we used two external fan heaters (FHs) located at both ends of the chamber blowing hot air perpendicularly to the propagating direction the optical beam and 20 temperature sensors positioned along the chamber to measure the temperature profile and thus C_n^2. Note that, the performance of a short laboratory FSO link can be equivalent to a longer outdoor FSO link by retaining the Rytov variance (σ_R^2). Details of the AT generation, σ_R^2 and C_n^2 levels processing can be found in [13].

The optical signal after the FSO link is amplified using an erbium doped fiber amplifier (EDFA–Keopsys CEFA-C-HG-SM-50-B130-FA-FA) with the pump power kept constant for all measurements with and without AT to maintain the same noise conditions for a fair comparison between different QAM formats. Following amplification, the optical signal is applied to a variable optical attenuator (VOA), which is used to vary the received optical power and corresponding P_{rRF} values at the receiving end. The transmission performance of each RF signal is comprehensively evaluated in terms of EVM, BER, signal-to-noise-ratio (SNR), P_{rRF} and constellation diagrams. Note that, P_{rRF} is the critical parameter for link performance evaluation since it is measured at the user equipment and used to estimate the achievable d under different weather conditions. Next, the two orthogonally polarized light waves are applied to the 3-tunable-knob PC-3 and PBS and then detected by two different PDs (i.e., PD-1–Optilab PD-40 and PD-2–New Focus 1554-B), respectively. By properly controlling the PC-3, the CD-induced power fading can be optimized for $x_1(t)$ and $x_2(t)$, resulting in enhanced recovered RF power, clear constellation diagrams and low EVMs. Note that, the measured optical power at both PD inputs is approximately 0 dBm.

The output of the PD-1 is further amplified using a cascaded PAs (PA-2–Miteq AMF-4F-260400-40-10p and PA-3–Analog device HMC1131) prior to being transmitted over a 2 m RF wireless channel using a pair of double ridged waveguide horn ANTs (Tx ANT-1 and Rx ANT-1–RFSpin DRH40). The output of the PD-2 is also amplified using a PA-4 (Mini circuits ZVA-213-S+) for transmission over a 2 m RF wireless link using pair of double ridged waveguide horn ANTs (Tx

TABLE 1
Key Parameters used in Experiments

Parameter			Value
Optical domain	Laser	Wavelength	1550 nm
		Output power	15 dBm
	SMF	Length and attenuation	20 km and 0.2 dB/km
		Chromatic dispersion	17 ps/(nm·km)
	FSO	Collimator aperture	24 mm
		Length and loss	4.2 m and 8 dB
	EDFA	Output power	7.2 dBm
		Noise figure	< 5 dB
$x_1(t)$, $(x_2(t))$	Carrier frequency		25 GHz **(2.6 GHz)**
	Modulation format		4/16/64-QAM **(4/16-QAM)**
	Bit rate		40/80/120 Mb/s **(34/68 Mb/s)**
	PD-1 **(PD-2)**	Responsivity	0.8 A/W **(0.85 A/W)**
		Bandwidth	33 GHz **(12 GHz)**
	PA-2 **(PA-4)**	Gain	22 dB **(26 dB)**
		Noise figure	1.7 dB **(3 dB)**
		Bandwidth	$24-27$ GHz **($0.8-21$ GHz)**
	PA-3	Gain	27 dB
		Noise figure	2 dB
		Bandwidth	$18-26.5$ GHz
	ANT-1 **(ANT-2)**	Frequency range	$4-40$ GHz **($0.74-10.5$ GHz)**
		Gain	15 dBi **(11 dBi)**
		Wireless channel length	2 m **(2 m)**

ANT-2 and Rx ANT-2–RFSpin DRH10). The received mmW and sub-6 GHz signals are captured using a signal and spectrum analyzer (SSA–R&S FSW) for performance evaluation. Note that, (*i*) all ANTs are fixed at the height of 1 m for the ideal alignment to maximize the signal strength at the Rx, (*ii*) the separation of two Tx ANTs and two Rx ANTs is 12 cm, and (*iii*) transmitting and receiving ANTs are in line-of-sight and operating at different frequency regions in order to minimize the interchannel interference. All the key system parameters adopted in the experimental setup are summarized in Table 1.

4. Experimental Results and Discussion

4.1 Link Performance of PDM-MPL (SMF and RF Wireless)

We first evaluate the link performance in terms of EVMs and BERs as a function of P_{rRF} for the 25 GHz mmW signal with 16-QAM i.e., $x_1(t)$ for OB2B + 2 m RF wireless link (denoted as OB2B) and 20 km SMF with a 2 m RF wireless link (denoted as PDM-MPL) as shown in Fig. 6.

As shown in Fig. 6(a), for OB2B and PDM-MPL the lowest EVM values are 2.1 and 5.4% at P_{rRF} of −44 and −55 dBm, respectively. A corresponding 16-QAM constellation for OB2B is clearly observed, as can be seen in the inset. The resultant RF power reduction between OB2B and PDM-MPL is attributed to the loss of the 20 km SMF since the EDFA is not used in this case. Also shown is the required limit of 12.5% EVM for 16-QAM according to 3rd generation partnership project (3GPP) standard [24]. Noticeably, almost no RF power penalty is observed at the EVM required limit. This is because the polarization misalignment and CD-induced power fading are
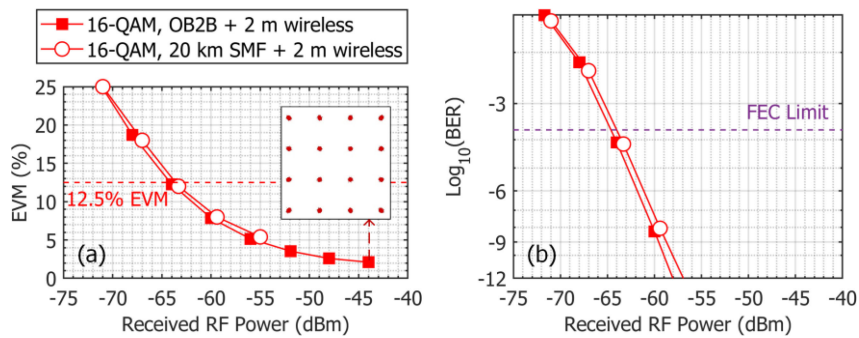
Fig. 6. (a) Measured EVMs and (b) calculated BERs versus received RF power for 25 GHz signal with 16-QAM format. Inset is the constellation obtained at $P_{rRF-Max}$ for OB2B.
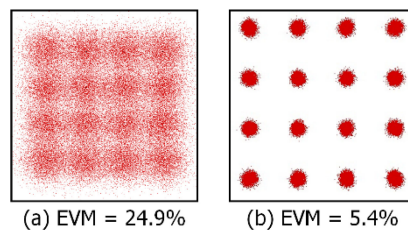

(a) EVM = 24.9%   (b) EVM = 5.4%

Fig. 7. The constellation diagrams of the received 25 GHz signal with 16-QAM: (a) before and (b) after optimization of CD-induced power fading.
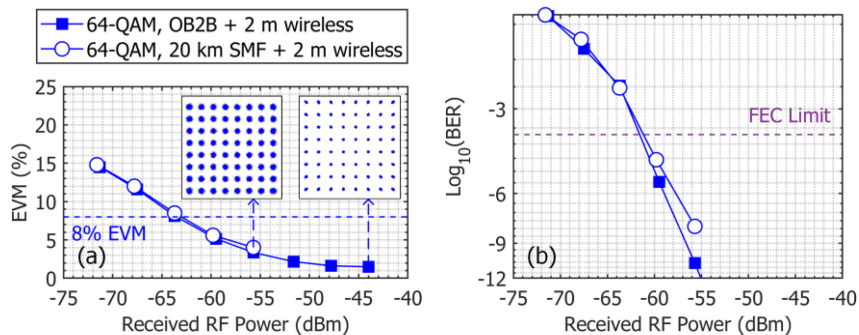

Fig. 8. (a) Measured EVMs and (b) calculated BERs versus the received RF power for 25 GHz 64-QAM. Insets are the constellations obtained at $P_{rRF-Max}$ for OB2B and PDM-MPL.

optimized by properly controlling the PC-3 as we have described in Section 2. The BER versus P_{rRF} is depicted in Fig. 6(b) based on the EVM-BER relationship for M-QAM as given in [13]. We see that, the BERs of the 16-QAM signal for OB2B and PDM-MPL cases are lower than the BER of 1×10^{-12} for P_{rRF} larger than -58 dBm, which indicates error-free transmissions. Comparing at the FEC limit of 2×10^{-4}, both cases are met at P_{rRF} of -64.5 dBm.

To demonstrate the mitigation of CD-induced power fading, we have determined the constellation diagrams before and after the optimization for the PDM-MPL, as shown in Figs. 7(a) and (b), respectively. As can be clearly seen, without optimization the constellation diagram is highly distorted, thus leading to a high EVM of 24.9%, which is well above the required EVM limit of 12.5%. With optimization, the constellation diagram is clear and stable with the EVM of 5.4%, i.e., considerably less than 12.5% limit.
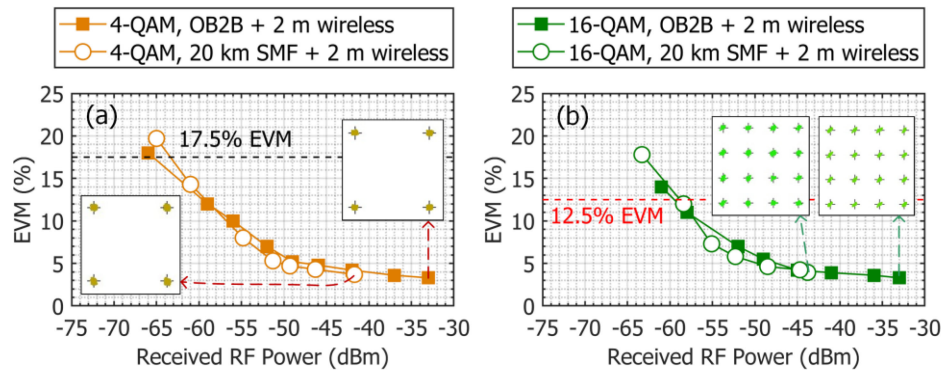
Fig. 9. Measured EVMs versus the received RF power for 2.6 GHz with (a) 4-QAM and (b) 16-QAM. Insets are the constellations obtained at $P_{rRF-Max}$ for OB2B and PDM-MPL.

Similarly, the results for the mmW signal with 64-QAM are shown in Fig. 8. For OB2B and PDM-MPL, the best EVM values are 1.5 and 4%, which are below the 8% EVM requirement for 64-QAM [24], at P_{rRF} of -44 and -56 dBm, respectively, see Fig. 8(a). For PDM-MPL, following compensation of the CD-induced power fading, P_{rRF} has been well recovered, which therefore results in a discernable 64-QAM constellation, see inset. In addition, no RF power penalty is observed in comparison to OB2B, confirming also the effectiveness of the optimization technique for higher-order QAM. As for the BER performance, an error-free transmission (i.e., BER $< 1 \times 10^{-12}$) is observed for OB2B, see Fig. 8(b). While the best BER for PDM-MPL is about 1.4×10^{-8}, which is well below the FEC threshold. Comparing at the FEC limit, both cases are met at P_{rRF} of -61.5 dBm. Relating to the 16-QAM signal in Fig. 6(b), we observe only 3 dB RF power penalty when changing from 16- to 64-QAM format. The performance of 64-QAM is worse than 16-QAM signal regardless of transmission scenarios owing to the fact that the SNR requirement is more stringent for higher-order modulation, that is investigated in the next sub-section.

We have further evaluated the EVM performance for $x_2(t)$ with 4- and 16-QAM format for both OB2B and PDM-MPL configurations, as shown in Fig. 9. As illustrated, for 2.6 GHz 4- and 16-QAM the measured EVMs are well below the EVM limits over a wide range of P_{rRF}. Note that, the performance of lower frequency bands is superior compared with $x_1(t)$ due to the lower signal propagation losses.

In detail, under OB2B, the 2.6 GHz 4- and 16-QAM signals have the lowest EVM of 3.3% measured at the maximum P_{rRF} of -33 dBm. For the 2.6 GHz 16-QAM signal at P_{rRF} of -44 dBm, the measured EVM is 4.1%, which is about 2% higher than that of $x_1(t)$, see Fig. 6(a). For the 2.6 GHz 16-QAM signal at P_{rRF} of -44 dBm, the measured EVM is 4.1%, which is about 2% higher than that of $x_1(t)$, see Fig. 6(a). This agrees well with the simulation results in Section 2 since $x_1(t)$ has a higher input RF power. Comparing between PDM-MPL and OB2B configuration, almost no RF power penalty is observed for each signal. Based on the measured EVMs, the resultant BERs are also calculated with the values well below the BER of 10^{-12}, which indicate error-free transmissions for $x_2(t)$ with both 4- and 16-QAM formats. The received constellation diagrams for all cases are depicted in the insets. The practicality of the proposed PDM-based system for the co-transmission and optimization of the CD-induced power fading for 25 and 2.6 GHz wireless signals is therefore validated.

4.2 Link Performance of PDM-HMPL (Hybrid SMF-FSO and RF Wireless)

In this section, we investigate the performance of PMD-HMPL (i.e., a hybrid optical channel of 20 km SMF and 4.2 m FSO) without and with AT and a 2 m RF wireless link (denoted as PDM-HMPL).
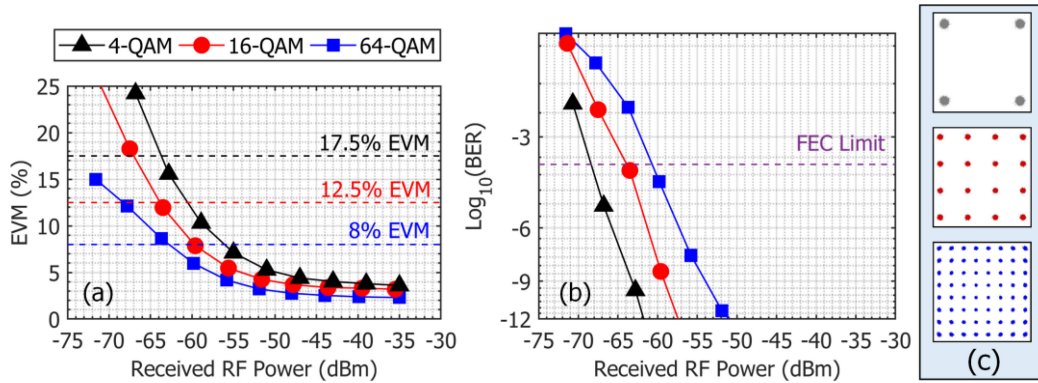
Fig. 10. (a) Measured EVMs and (b) calculated BERs versus the received RF power for 25 GHz with 4/16/64-QAM. (c) Constellation diagrams obtained at $P_{\text{rRF−Max}}$ for PDM-HMPL without AT.
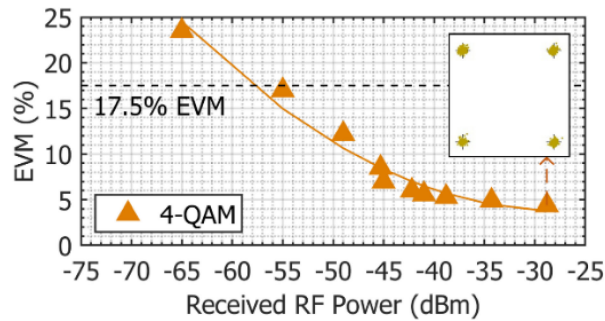

Fig. 11. Measured EVMs versus the received RF power for 2.6 GHz with 4-QAM. Inset is the constellation diagram at $P_{\text{rRF−Max}}$ for PDM-HMPL without AT.

4.2.1. Measurements Without AT: Fig. 10(a) shows the post-optimization EVM as a function of P_{rRF} for $x_1(t)$ with 4-, 16- and 64-QAM under no AT i.e., C_n^2 is 2.59×10^{-14} m$^{-2/3}$. As shown, the EVM plots display exponential drop with P_{rRF} having the lowest EVM values of 3.6, 3.2 and 2.3% at P_{rRF} of -35 dBm for 4-, 16- and 64-QAM, respectively. Note that, the extended P_{rRF} range (i.e., lower EVMs) is due to the use of EDFA. The BER plots for 4-, 16- and 64-QAM are illustrated in Fig. 10(b) together with the FEC limit. The lowest EVM values of 3.6, 3.2 and 2.3% correspond to error-free transmissions i.e., BER of less than 10^{-12}. The constellation diagrams at P_{rRF} of -35 dBm for QAM signals are also displayed in Fig. 10(c), which are clear and stable. Compared with 64-QAM in OB2B, see Fig. 8(a), at P_{rRF} of -44 dBm we observe the EVM penalty of 1%, which demonstrates the benefit of adopting FSO in ODN.

For $x_2(t)$ in PDM-HMPL, we have evaluated only the microwave vector signal with 4-QAM. The EVM performance is given in Fig. 11. As expected, the lowest EVM is 4.4% at P_{rRF} of -28.8 dBm with a clear constellation shown in the inset, thus demonstrating full recovery of the 2.6 GHz signal following optimization. In comparison to 4-QAM in OB2B, see Fig. 9(a), at P_{rRF} of -33 dBm, the EVM penalty is only 1%, which indicates the practicality of the proposed HMPL for the co-transmission of mmW and sub-6 GHz wireless signals.

To further evaluate the proposed PDM-HMPL as part of the future converged mmW and sub-6 GHz RATs, we measured the EVM values and then converted them to BERs as a function of the electrical SNR for both 25 GHz 4/16/64-QAM and 2.6 GHz 4-QAM signals under no AT, see Fig. 12(a) and (b), respectively. All cases show the best BERs below the FEC threshold. For the 25 GHz signal, the minimum SNR required for 4-QAM to satisfy the FEC limit is about 16.5 dB.
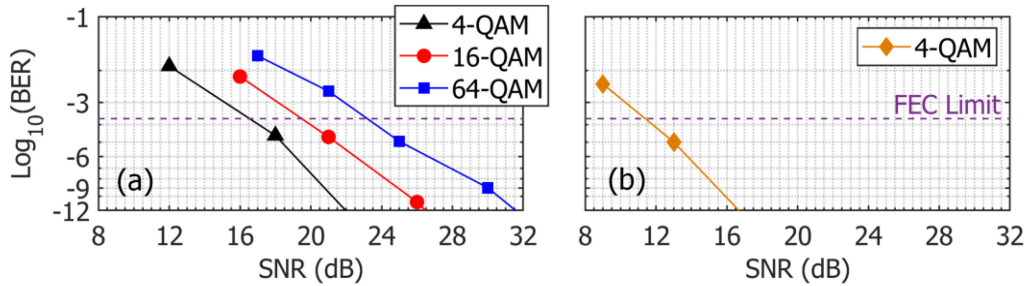
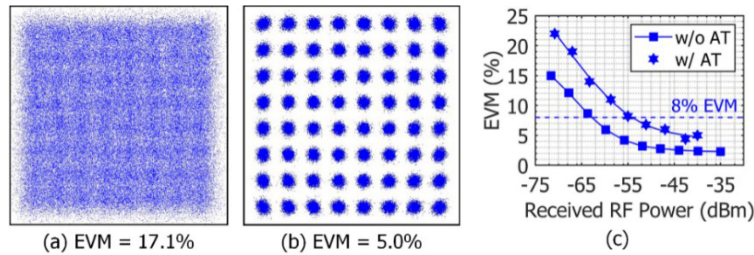Fig. 12. Calculated BERs versus SNR at the Rx for: (a) 25 GHz with 4/16/64-QAM and (b) 2.6 GHz with 4-QAM.

Fig. 13. The constellation diagram of the received 25 GHz with 64-QAM: (a) before and (b) after the optimization of the power fading. (c) Measured EVMs versus P_{rRF}.

While that of 16- and 64-QAM are about 19.5 and 23.5 dB leading to 3 and 7 dB more in comparison to 4-QAM. For the 2.6 GHz signal, the required SNR for 4-QAM is only 11.5 dB, which is 5 dB lower than that of 25 GHz 4-QAM signal since it is operated in the sub-6 GHz frequency band.

4.2.2. Measurements With AT: In this case, we examine only $x_1(t)$ with 64-QAM under AT. After offline processing the recorded temperature profile based on Equations (2) and (3) in [13], the σ_R^2 and C_n^2 are calculated about 0.011938 and 1.49×10^{-11} m$^{-2/3}$, respectively. As expected, the joint effect of CD- and AT-induced power fading significantly limits the performance of the mmW wireless service, as seen from the constellation diagram in Fig. 13(a). The constellation diagram is highly distorted due to the strong correlation between adjacent symbols, which results in a high EVM level of 17.1% (i.e., higher than the required EVM limit) and a corresponding BER of 5.9×10^{-2} (i.e., above the FEC threshold). The CD-induced power fading, however, can be separately optimized regardless of the AT-induced power fading through properly controlling the PC-3. Following optimization, P_{rRF} is recovered, which, in turn, leads to an improved constellation diagram with a low EVM of 5.0% (i.e., lower than the required EVM limit) as depicted in Fig. 13(b) and the corresponding BER of 3.7×10^{-6} (i.e., below the FEC threshold). The EVM and BER performance of the 25 GHz mmW with 4- and 16-QAM can also be expected to satisfy the requirements.

Finally, Fig. 13(c) shows the EVM dependency on P_{rRF} for the link with and without AT. Note that, under AT, the propagating optical signals experience a higher degree of intensity and phase fluctuations, thus leading to the fluctuations in EVM. We observe that, with AT, the best EVM achieved is 5.0% and the corresponding BER is 3.7×10^{-6}. However, in contrast to the link without AT, the EVM quickly fails to meet the EVM criterion of 8% for $P_{rRF} < -54$ dBm, while that of without AT is -63 dBm, see Fig. 10(a), which leads to a 9 dB RF power penalty. This shows clearly the power fading due to the effect of strong AT in FSO. At P_{rRF} of -44 dBm, the measured EVM is 5.2%, thus resulting in the EVM penalty of 3.7% compared with 64-QAM in OB2B, see Fig. 8(a). It is worth mentioning that by remaining the same σ_R^2 of 0.011938, the short indoor FSO link under

strong C_n^2 of 1.49×10^{-11} m$^{-2/3}$ is equivalent to the outdoor FSO link length of 760 m under the practical C_n^2 of 10^{-15} m$^{-2/3}$. This shows the viability of real-world implementation of the proposed PDM-HMPL with 20 km SMF and up to 760 m FSO for use in converged mmW and sub-6 GHz RATs. The performance of $x_2(t)$ signal with different QAM formats can also be anticipated to satisfy the requirements. In order to maximize the signal quality of both mmW and sub-6 GHz wireless services in a long-term practical implementation of the proposed PDM-HMPL, an adaptive digital PC should replace the PC-3 for an automatic optimization.

5. Conclusion

In this paper, a hybrid microwave photonic link containing a SMF and FSO under the AT using a PDM-MZM with the optimization of the CD-induced power fading regardless of the AT-induced power fading is proposed to support the co-existence of mmW and sub-6 GHz RAT. We first carried out in simulation the co-transmission of the multi-Gb/s intensity-modulated 25 and 2.6 GHz 4-QAM signals. The numerical simulation allowed us to obtain the optical and electrical spectra at different nodes of the proposed converged mmW and sub-6 GHz RATs and analyze the impact of CD-induced power fading on both multi-Gb/s link performances. We also showed the effectiveness of optimizing the single PC at the Rx to compensate for the relative phase changes between the optical carrier and the sidebands as they propagate over SMF, which, in turn, mitigates the CD-induced power fading. We then experimentally demonstrated the simultaneous transmission of both signals over a hybrid optical channel consisting of a 20 km SMF and 4 m FSO under the AT effect to comprehensively observe the impact of power fading due to CD and AT. After optimization, we achieved no performance degradation caused by the CD with the measured EVMs and predicted BERs for both signals using the optical DSB modulation. We also showed that, FSO link length can be equivalently extended up to 760 m in outdoor environments with a typical AT of 10^{-15} m$^{-2/3}$, which is adequate to cover ultra-dense, hotspot areas and emergency situations. As an advantage, the proposed PDM-based system can be reused to implement the transmission of both signals with the identical mmW carrier frequency, which therefore offers (*i*) high-capacity and (*ii*) seamless 2×2 multiple-input multiple-output transmissions for future wireless networks.

References

[1] "In the matter of expanding flexible use in the 3.7–4.2 GHz band," 2020. [Online]. Available: https://www.fcc.gov/document/fcc-expands-flexible-use-c-band-5g-0
[2] "5G spectrum GSMA public policy position," 2020. [Online]. Available: https://www.gsma.com/
[3] L. Wei, R. Hu, Y. Qian, and G. Wu, "Key elements to enable millimeter wave communications for 5G wireless systems," *IEEE Wirel. Commun.*, vol. 21, no. 6, pp. 136–143, Dec. 2014.
[4] "FCC takes steps to facilitate mobile broadband and next generation wireless technologies in spectrum above 24 GHz," 2016. [Online]. Available: https://www.fcc.gov/document/fcc-adopts-rules-facilitate-next-generation-wireless-technologies
[5] Z. Pi and F. Khan, "An introduction to millimeter-wave mobile broadband systems," *IEEE Commun. Mag.*, vol. 49, no. 6, pp. 101–107, Jun. 2011.
[6] X. Li, J. Yu, and G.-K. Chang, "Photonics-aided millimeter-wave technologies for extreme mobile broadband communications in 5G," *J. Lightw. Technol.*, vol. 38, no. 2, pp. 366–378, Jan. 2020.
[7] C. Lim, Y. Tian, C. Ranaweera, A. Nirmalathas, E. Wong, and K. Lee, "Evolution of radio-over-fiber technology," *J. Lightw. Technol.*, vol. 37, no. 6, pp. 1647–1656, Mar. 2019.
[8] H. Y. Wang, C. H. Cheng, C. T. Tsai, Y. C. Chi, and G. R. Lin, "28-GHz wireless carrier heterodyned from orthogonally polarized tri-color laser diode for fading-free long-reach MMWoF," *J. Lightw. Technol.*, vol. 37, no. 13, pp. 3388–3400, Jul. 2019.
[9] X. Chen and J. Yao, "Data rate quadrupled coherent microwave photonic link," *IEEE Photon. Technol. Lett.*, vol. 29, no. 13, pp. 1071–1074, Jul. 2017.
[10] E. Martin *et al.*, "28 GHz 5G radio over fibre using UF-OFDM with optical heterodyning," in in *Proc. Int. Top. Meet. Microw. Photon.*, 2017, Paper. Th2.4.
[11] Y. Chen, J. Xiao, and Z. Dong, "Delivering dual polarization-division-multiplexing millimeter-wave signals at W-Band by one pair of antennas," *IEEE Photon. J.*, vol. 11, no. 5, pp. 1–10, 2019.
[12] X. Li *et al.*, "Delivery of 54-Gb/s 8QAM W-band signal and 32-Gb/s 16QAM K-band signal over 20-km SMF-28 and 2500-m wireless distance," *J. Lightw. Technol.*, vol. 36, no. 1, pp. 50–56, Jan. 2018.

[13] D.-N. Nguyen, J. Bohata, M. Komanec, S. Zvanovec, B. Ortega, and Z. Ghassemlooy, "Seamless 25 GHz transmission of LTE 4/16/64-QAM signals over hybrid SMF/FSO and wireless link," *J. Lightw. Technol.*, vol. 37, no. 24, pp. 6040–6047, Dec. 2019.

[14] P. T. Dat, A. Kanno, N. Yamamoto, and T. Kawanishi, "Full-duplex transmission of LTE-A carrier aggregation signal over a bidirectional seamless fiber-millimeter-wave system," *J. Lightw. Technol.*, vol. 34, no. 2, pp. 691–700, Jan. 2016.

[15] J. Zhang *et al.*, "Full-duplex quasi-gapless carrier aggregation using FBMC in centralized radio-over-fiber heterogeneous networks," *J. Lightw. Technol.*, vol. 35, no. 4, pp. 989–996, Feb. 2017.

[16] R. M. Borges *et al.*, "Integration of a GFDM-based 5G transceiver in a GPON using radio over fiber technology," *J. Lightw. Technol.*, vol. 36, no. 19, pp. 4468–4477, Oct. 2018.

[17] L. Huang *et al.*, "Simple multi-RAT RoF system with 2 × 2 MIMO wireless transmission," *IEEE Photon. Technol. Lett.*, vol. 31, no. 13, pp. 1025–1028, Jul. 2019.

[18] W. Zhang, A. Wen, Y. Li, and J. Ma, "A high spectral efficiency microwave photonic link with optimization of chromatic-dispersion-induced power fading," *J. Lightw. Technol.*, vol. 37, no. 4, pp. 1123–1132, Feb. 2019.

[19] Z. Ghassemlooy, W. O. Popoola, and S. Rajbhandari, in *Optical Wireless Communications–System and Channel Modelling With Matlab*. 2nd ed. Boca Raton, FL, United States: CRC Press, 2019.

[20] L. Li *et al.*, "Mitigation for turbulence effects in a 40-Gbit/s orbital-angular-momentum-multiplexed free-space optical link between a ground station and a retro-reflecting UAV using MIMO equalization," *Opt. Lett.*, vol. 44, no. 21, Nov. 2019, Art. no. 5181.

[21] R. Zheng, E. H. W. Chan, X. Wang, X. Feng, and B. Guan, "Broadband high dynamic range fiber optic link based on a dual-polarization modulator," *Opt. Express*, vol. 27, no. 4, 2019, Art. no. 4734.

[22] K. Van Gasse *et al.*, "III-V-on-silicon photonic transceivers for radio-over-fiber links," *J. Lightw. Technol.*, vol. 36, no. 19, pp. 4438–4444, Oct. 2018.

[23] H. Kaushal and G. Kaddoum, "Optical communication in space: Challenges and mitigation techniques," *IEEE Commun. Surv. Tutorials*, vol. 19, no. 1, pp. 57–96, Jan./Mar. 2017.

[24] 3GPP TS 36.104. "Base station (BS) radio transmission and reception," 2018.